



Cite this: DOI: 10.1039/c9nr04355a

Magneto-mechanical actuation of magnetic responsive fibrous scaffolds boosts tenogenesis of human adipose stem cells†

Ana R. Tomás,^{a,b} Ana I. Gonçalves,^{a,b} Elvira Paz,^c Paulo Freitas,^c Rui M. A. Domingues  ^{*a,b,d} and Manuela E. Gomes  ^{*a,b,d}

Tendons are highly specialized load-bearing tissues with very limited healing capacity. Given their mechanosensitive nature, the combination of tendon mimetic scaffolds with remote mechanical actuation could synergistically contribute to the fabrication of improved tissue engineered alternatives for the functional regeneration of tendons. Here, hybrids of cellulose nanocrystals decorated with magnetic nanoparticles were produced to simultaneously reinforce and confer magnetic responsiveness to tendon mimetic hierarchical fibrous scaffolds, resulting in a system that enables remote stimulation of cells *in vitro* and, potentially, *in vivo* after construct transplantation. The biological performance and functionality of these scaffolds were evaluated using human adipose stem cells (hASCs) cultured under or in the absence of magnetic actuation. It was demonstrated that magneto-mechanical stimulation of hASCs promotes higher degrees of cell cytoskeleton anisotropic organization and steers the mechanosensitive YAP/TAZ signaling pathway. As feedback, stimulated cells show increased expression of tendon-related markers, as well as a pro-healing profile in genes related to their inflammatory secretome. Overall, these results support the use of the proposed magnetic responsive fibrous scaffolds as remote biointegrated actuators that can synergistically boost hASC tenogenesis through mechanosensing mechanisms and may modulate their pro-healing paracrine signaling, thus collectively contributing to the improvement of the regenerative potential of engineered tendon grafts.

Received 21st May 2019,
Accepted 3rd September 2019
DOI: 10.1039/c9nr04355a
rsc.li/nanoscale

1. Introduction

Tendons are dense connective tissues that allow an effective transmission of forces between muscles and bones enabling skeletal movement.¹ Their vital role in the overall functioning of the musculoskeletal system prompts tendons to injuries that affect the quality of life of individuals of all ages, with over 30 million new cases of tendon and ligament related injuries being reported annually worldwide.²

Tendons are characterized by an abundant extracellular matrix (ECM), composed mostly of type I collagen, that is maintained by a small resident cell population of tenocytes and a low number of stem/progenitor cells.³ The tendon ECM has a well-organized hierarchical architecture formed predominantly of fibrous structures parallelly assembled from the nano- (collagen fibrils, 20–150 nm) up to the macro-scale (fascicles, 1000–3000 μm).^{3,4} Their longitudinal alignment ensures that tendons can sustain extremely high tensile forces, while their hierarchical structure is responsible for the viscoelastic behavior that endows tendons with shock-absorbing properties at low strains.^{5,6} The natural healing capacity of these tissues is however highly limited by their hypovascular and hypocellular nature and the disordered ECM deposited after injury forms scar tissue^{1,7} with inferior biomechanical properties that is more prone to re-injury or leads to chronic disorders.^{8,9}

Currently, tendon injuries and pathologies are managed through conservative approaches or, in more severe cases, through surgical intervention.^{2,10} However, to date none of these treatments has been able to fully restore tendon functionality prior to injury, regardless of its severity.⁹ In recent years, tissue engineering (TE) approaches have been proposed

^a3B's Research Group, I3Bs-Research Institute on Biomaterials, Biodegradables and Biomimetics, University of Minho, Headquarters of the European Institute of Excellence on Tissue Engineering and Regenerative Medicine, AvePark, Parque de Ciência e Tecnologia Zona Industrial da Gandra, Barco, Guimarães 4805-017, Portugal. E-mail: rui.domingues@i3bs.uminho.pt, megomes@i3bs.uminho.pt

^bICVS/3B's – PT Government Associate Laboratory, Braga/Guimarães, Portugal

^cINL – International Iberian Nanotechnology Laboratory, Av. Mestre José Veiga, Braga, 4715-330, Portugal

^dThe Discoveries Centre for Regenerative and Precision Medicine, Headquarters at University of Minho, Avepark, Barco, Guimarães 4805-017, Portugal

†Electronic supplementary information (ESI) available: Additional characterization of magnetic nanoparticles and of electrospun fibrous constructs. Magnetic nanoparticles production methods. See DOI: 10.1039/c9nr04355a

as therapeutic alternatives to address this challenge.^{2,9} Electrospinning, in particular, has been among the preferred manufacturing techniques for fiber-based scaffolds for tendon TE.^{5,11,12} We have recently devised a novel system for the scalable production of 3D woven scaffolds based on the assembly of continuous and aligned electrospun nanofibre threads that mimicked the aligned topography and nano-to-macro hierarchy of the tendon's fibrous architecture, as well as its non-linear biomechanical behavior.¹³ Remarkably, the physical cues of these scaffolds could self-support the maintenance of tenocytes' phenotype and induce the tenogenic commitment of adipose derived stem cells in the absence of biological factor supplementation.

Nevertheless, as mechanosensitive tissues, physiological loads are fundamental for the maintenance of tendon homeostasis.^{6,14} In fact, it has been shown that cells can adapt their behavior in terms of differentiation,¹⁵ matrix protein synthesis¹⁶ or even healing mechanisms¹⁷ in response to external mechanical stimuli through mechanotransduction.¹⁸ Strain-based bioreactors have been typically used to emulate physiological conditions and mechanically stimulate cells in tendon tissue engineered constructs.^{19,20} However, these methods are limited to *in vitro* settings that cannot be continued *in vivo* after construct transplantation to promote neo-tissue formation and effective integration with the host tissue. Moreover, the use of bioreactors with very specific designs, and limited number of chambers or that requires attachment of the construct to mechanical stretchers to apply strains, which might themselves induce significant damages on cultured cells,²¹ are limitations of these approaches. Therefore, the development of biomimetic scaffolds that can be synergistically used as remote biointegrated actuators would represent a significant advance in the field. It would not only facilitate the mechanical stimulation of the tissue engineered construct during its *in vitro* maturation as it would also open the possibility to continue to deliver that stimuli *in vivo* after transplantation, boosting the regenerative potential of the proposed system.

Magnetic fields can be used as exogenous mechanical triggers of magnetic responsive scaffolds to exert forces over seeded cells without directly targeting membrane receptors and ion channels.²² Polymeric composites incorporating magnetic nanoparticles (MNPs), particularly superparamagnetic iron oxide, are among the preferred remotely actuatable biomaterials.²³ In principle, the local substrate deflections caused by actuation of MNPs in response to an external magnetic force²⁴ can create transient physical forces that are transferred to cells present in close proximity to the nanoparticles and should be able to activate/promote mechanotransduction mechanisms that would ultimately drive cellular responses towards the desired behavior.^{18,22,25} Magnetic stimuli combined with magnetic responsive scaffolds have shown positive results in vascular,²⁶ cardiac,²⁷ neural,²⁸ skeletal muscle²⁹ and bone^{30–33} TE strategies. Our group has recently reported on 3D plotted scaffolds for tendon TE, suggesting their improved biological performance in comparison with non-magnetically

stimulated equivalents.³⁴ Furthermore, we and others have demonstrated the immunomodulatory potential of magnetic responsive biomaterials under magnetic stimulation conditions,^{31,35} a functionality that is highly relevant in the context of tendon regeneration given the importance of managing the inflammatory response in the treatment of tendinopathy.³⁶

However, to date, magnetic responsive scaffold systems that can closely mimic the 3D microstructural and architectural features of native tissues, key parameters to achieve the characteristic cellular organization and biomechanical behavior of tendon tissues in TE approaches, have not been reported. Moreover, since both the topographical cues and mechanical stimulation are strong regulators of mechanosensitive cell functions, the knowledge on how magneto-mechanical actuation of tendon mimetic scaffolds synergistically feedback on cells' mechanotransduction remains an elusive subject.

Building on our previously developed fabrication approach,¹³ here we propose a new magnetic responsive 3D fibrous scaffold that closely mimics the hierarchical architecture and biomechanical behavior of native tendons to create an artificial niche potentially capable of magneto-mechanically stimulating cells on demand, both *in vitro* and *in vivo*. For this purpose, continuous and aligned electrospun fiber threads were fabricated based on a poly- ϵ -caprolactone (PCL) matrix filled with hybrid rod-shaped cellulose nanocrystals (CNCs) decorated with iron oxide MNPs (MNP@CNC) to confer simultaneous mechanical reinforcement and magnetic responsiveness. 3D hierarchical scaffolds were produced by assembling the electrospun fiber threads through textile techniques. The biological performance and functionality of the system were assessed by culturing hASCs under the influence or absence of magnetic stimuli. We focused particularly on evaluating how the scaffolds' biophysical cues and magneto-mechanical actuation synergistically affect cytoskeleton organization and key mechanotransducers, and on how these signals perceived by the cell through the cytoskeleton influence their capacity to induce the tenogenic differentiation of stem cells.

2. Experimental section

2.1. Materials

Avicel® PH-101 microcrystalline cellulose (MCC), 1-dodecanethiol (1-DT), dopamine hydrochloride, triethylamine, tris ((hydroxyethyl)aminomethane), collagenase type II (C6885) and phalloidin tetramethylrhodamine B isothiocyanate were purchased from Sigma-Aldrich, Portugal. Poly- ϵ -caprolactone (PCL, average M_n 80 000) was purchased from Sigma-Aldrich, UK. Ammonium hydroxide solution, iron(II) chloride tetrahydrate, iron(III) chloride hexahydrate and sulfuric acid (95–97%) were obtained from Honeywell Fluka™, Germany. Tetrahydrofuran GPC grade (THF) and *N,N*-dimethylformamide (DMF) were purchased from AppliChem, Germany, and Thermo Fisher Scientific, UK, respectively. Antibiotic/antimycotic solution (A/A), minimum essential medium alpha

(α -MEM), and phosphate buffered saline (PBS) were purchased from Life Technologies, UK, and fetal bovine serum (FBS) from Life Technologies, Netherlands. 10% Neutral buffered formalin and Alexa Fluor® 488 (A21202) were obtained from Thermo Fisher Scientific, USA, and TritonX-100™ from Thermo Fisher Scientific, Belgium. Anti-collagen I (COL1A1, ab90395), anti-SCXA-aminoterminal end (ab58655) and anti-osteocalcin (OCN, ab13418) antibodies were obtained from abcam, UK. YAP/TAZ (sc-101199) antibody was purchased from Santa Cruz Biotechnology, Germany, and the polyclonal tenomodulin (TNMD) antibody was kindly produced and provided by Prof. Denitsa Docheva, University of Regensburg, Germany. Antibody diluent with background reducing components was purchased from Dako, Denmark, RTU normal horse serum from Vector Laboratories, UK, and 4,6-diamidino-2-phenylindole dilactate (DAPI) from Biotium, USA. CellTiter 96® Aqueous One Solution (MTS Assay) was obtained from Promega, USA, and RiboZol (RNA extraction reagent) from VWR, USA. PerfeCTa SYBR Green FastMix and a qScript cDNA Synthesis Kit were purchased from Quanta Biosciences, USA.

2.2. Production of magnetic nanoparticles

CNCs were produced through sulfuric acid hydrolysis of MCC (see the ESI, Method 2.1†) and then decorated with iron oxide MNPs (MNP@CNC) through *in situ* co-precipitation of Fe²⁺ and Fe³⁺ (see the ESI, Method 2.2†), as previously described.³⁷ MNP@CNC were then coated with thin layers of polydopamine (PDA) and further grafted with 1-DT (see the ESI, Method 2.3†).

2.3. Nanoparticle characterization

The morphology and dimensions of the produced nanoparticles were assessed by atomic force microscopy (AFM, Dimension Icon, Bruker, Germany) and scanning transmission electron microscopy (STEM, Auriga Compact, Zeiss, Germany) analysis. For AFM, drops of the diluted nanoparticle solutions (0.0015 wt%) were deposited on freshly cleaved mica discs, and dried and then images were acquired in tapping mode with a range of $xy - 1$ nm to 90 μ m, and analyzed using Gwyddion software (version 2.49) to obtain the CNC length and height ($n = 280$). For STEM, drops of the diluted suspensions were placed in TEM grids (Carbon Type B, 400 M Cu, Monocomp), and images were acquired at an acceleration voltage of 25–30 kV. Fourier Transform Infrared (FTIR, IRPrestige 21, Shimadzu, Japan) spectra were obtained to assess the chemical composition and to confirm the successful building of the coating on the produced nanoparticles. For this, nanoparticles were pelleted with KBr and spectra were acquired within 400–4000 cm^{-1} , with 32 scans per sample and a resolution of 4 cm^{-1} . The magnetic properties of the produced magnetic hybrid nanoparticles, (MNP@CNCs and coated MNP@CNCs), were evaluated using a superconducting quantum interference device (SQUID-VSM) magnetometer (Quantum Design, USA). Freeze-dried samples of each formulation were analyzed under a magnetic field up to 20 kOe at room temperature.

2.4. Fabrication of PCL/DT-NP continuous fiber threads

PCL/DT-NP electrospinning solutions were prepared with 17% (w/v) of PCL and by incorporating 2.5, 5 or 7.5% (w/w) DT-NP relatively to PCL mass (PCL/DT-NP2.5, PCL/DT-NP5 and PCL/DT-NP7.5, respectively). DT-NP were dispersed on a DMF/THF solution (1 : 1 (v/v)) and sonicated thrice (ultrasonic processor, VCX-130PB-220, Sonics, USA, 1 min per cycle) using an ultrasound probe at 40% amplitude output. PCL was added to the MNP@CNC suspension, which was then left stirring at room temperature for 3–4 h. Prior to use, the solution was again sonicated (3 cycles, 1 min per cycle), in an ice bath to prevent overheating and ensure the proper dispersion of all components. Continuous fiber threads were fabricated adopting our previously proposed customized electrospinning setup.¹³ Briefly, the PCL/DT-NP solution was loaded into a syringe with a 21 G needle and jetted, at a constant flow rate of 0.4 mL h^{-1} and under a voltage of 9 kV, towards a grounded water/ethanol liquid bath (8 : 2 (v/v)). Continuous fiber threads were pulled at constant speed from the surface of the bath, placed at 14 cm directly below the needle, with a roller located 20 cm from the needle, horizontally. The produced fiber threads were pulled at 0.24, 0.56, 0.73 or 0.86 cm s^{-1} winding speed, maintaining the room temperature at 24 ± 2 °C and 45–50% humidity.

2.5. Thread assembly into yarns and 3D scaffolds

The produced threads were assembled into yarns by twisting 12 threads together at 4 turns per cm. Yarns of PCL/DT-NP5 collected at 0.73 cm s^{-1} were then weaved into 3D scaffolds, as previously described.¹³ First, two rows of pins were placed 0.5 cm apart, with 2 mm between every pin from the same row. One yarn was laid down in an alternating zig-zag pattern between the pins, to support the scaffold's structure, and a second yarn was weaved through the former. After removing every pin, the support structure was tight and knotted at the end.

2.6. Characterization of fiber threads

High-Resolution Field Scanning Electron Microscopy (SEM, JSM-6010LV, JEOL, Japan) was used to assess the morphology, alignment and dimensions of the electrospun threads. Specimens were coated with approximately 2 nm of platinum (Cressington, UK) prior to imaging, and images were collected at an acceleration voltage of 10 kV. ImageJ software (version: 1.51f, NIH, USA) was used to measure thread and fiber diameters ($n = 50$). Fiber alignment in the produced threads was assessed through the directionality plugin (<https://imagej.net/Directionality>) from ImageJ. Directionality histograms were generated to translate the amount of structures in the image along an angle of orientation (-90 – 90°). Histograms of each condition ($n = 3$) were fitted with a Gaussian function using Origin Lab software (version: 9.0.0, OriginLab Corporation, USA). The peak height and full width at half maximum (FWHM) of the peaks from each condition were used to assess fiber alignment. The quality of the fitting was evaluated according to the value of adjusted R^2 , which ranges from 0, indicating a poor fit, to 1, indicating a good fit. For an average

R^2 value lower than 0.75, the FWHM of the peak was considered 180° , meaning the lack of any preferential domains of alignment.

Mechanical properties of yarns and scaffolds fabricated with different amounts of DT-NP were assessed using a universal mechanical testing machine (5543, Instron, UK) equipped with a 1 kN load cell. 3 cm long specimens of each yarn were cut and fixed in square paper frames with a 1×1 cm window ($n > 9$). These specimens were then mounted onto the tester grips at a gauge length of 1 cm. Before testing, the paper frames were cut laterally, and the test was performed at a cross-head speed of 10 mm min^{-1} . Images from each specimen were acquired with an optical microscope (Stemi 2000-C, Zeiss, Germany) for cross-sectional area calculations, prior to testing. The cross-sectional area was estimated from yarn diameter measurements at three different locations along the length of the specimen, which were obtained using ImageJ software. Analogously, for woven scaffolds, 2 cm long specimens were fixed in paper frames with a 0.5×1 cm window. These were then mounted onto the tester grips at a gauge length of 5 mm and the test was performed at a crosshead speed of 5 mm min^{-1} . Prior to testing, the dimensions of the specimens were measured using a digital caliper for cross-sectional area calculations. From the acquired data, the Young's modulus, the yield stress and strain, the ultimate tensile strength and the strain at break of each specimen were calculated using MATLAB software (R2015b, MathWorks, USA).

The magnetic properties of the PCL/DT-NP2.5 and PCL/DT-NP5 yarns were evaluated following the same method adopted to characterize magnetic nanoparticles.

2.7. Biological studies

Human adipose stem cells (hASCs) were isolated from liposuction aspirates, obtained from healthy females ($n = 3$) with an average age of 42 years, under previously established protocols with Hospital da Prelada (Porto, Portugal) and with informed consent of the patients. The content of the written informed consent and related procedures were reviewed and approved by the Hospital Ethics Committee. hASCs were isolated and cultured as previously described,^{38,39} and have been previously characterized by RT-PCR for CD44, STRO-1, CD105 and CD90 markers, and also for multilineage potential.^{38–40} Briefly, the tissue was rinsed in PBS containing 10% of an A/A solution. The fat solution was immersed in a 0.05% collagenase type II solution for 45 min at 37°C under mild agitation. The digested tissue was centrifuged at $800g$ for 10 min at 4°C , after which the supernatant was eliminated. Finally, cells were expanded in basic culture medium composed of α -MEM supplemented with 10% FBS and 1% A/A solution, and used at passage 3–4.

2.7.1. Cell seeding. Prior to cell seeding, the yarns were mounted onto CellCrown inserts (Sigma-Aldrich, USA). The insert mounted yarns or woven scaffolds were sterilized by immersion in 70% ethanol for 1 h. Then, samples were washed 4 times with PBS, to remove the remaining ethanol and immersed in basal culture medium composed of α -MEM

supplemented with 10% FBS and 1% A/A solution for 1 h. hASCs were suspended in culture media and seeded at a density of 5×10^4 cells per well for each yarn or of 15×10^4 cells onto each woven scaffold and incubated overnight under static conditions to allow cell adhesion. Samples were then transferred to a new plate and fresh culture medium was added to each well. Culture experiments were conducted under static (control group) and magnetic stimulating conditions (oscillation frequency of 2 Hz and 0.2 mm of horizontal displacement) for 21 days in a magnefect nano-device (nanoTherics Ltd, UK) consisting of an array of permanent magnets (arranged to fit under 24 well plates), each with a surface magnetic field of 0.35 T, as described by Gonçalves *et al.*, 2016.³⁴ The magnetic field strength at the samples' position inside the wells was of around 0.30 T, measured with a gaussmeter (GM08, Hirst Magnetic Instruments LTD, UK).

2.7.2. Cell metabolic activity. Cell metabolic activity of hASCs was evaluated by MTS assay after 11 and 21 days of culture. Constructs were rinsed in PBS and then incubated in a mixture of FBS-free culture medium without phenol red and MTS solution (5 : 1 ratio) for 3 h, at 37°C and under a 5% CO_2 atmosphere. Then, 100 μL of each sample was transferred to a new 96-well plate and the absorbance was read at 490 nm (Synergy HT, Bio-Tek Instruments, USA). The absorbance of each sample was measured in triplicate and blank readings were performed for correction purposes.

2.7.3. mRNA extraction and real-time RT-PCR. Total RNA was extracted from the constructs using RiboZol extraction reagent according to the manufacturer's instructions. RNA quantity and purity were determined with a NanoDrop ND-1000 spectrophotometer (NanoDrop, ThermoScientific, USA). The cDNA synthesis was performed with the qScript cDNA Synthesis kit and using the Mastercycler Realplex (Eppendorf, Germany) with a total RNA of 1 μg in a volume of 20 μL . The quantification of the transcripts was carried out by quantitative polymerase chain reaction (qPCR) using the PerfeCTA SYBR Green FastMix kit following the manufacturer's protocol, in a Real-Time Mastercycler Realplex thermocycler (Eppendorf, Germany). The primers were pre-designed with PerlPrimer v1.1.21 software (see the ESI, Table S4†) and synthesized by MWG Biotech. ACTB (actin beta) was used as the housekeeping gene. The $2^{-\Delta\Delta\text{Ct}}$ method was selected to evaluate the relative expression level for each target gene.⁴¹ All values were first normalized against ACTB values, and then to hASCs collected at day 0. Samples were collected and analyzed in triplicate.

2.7.4. Immunofluorescence. At 11 and 21 days, hASC constructs were rinsed with PBS and fixed with 10% neutral buffered formalin prior to the detection of YAP/TAZ, SCX and TNMD in yarns and TNMD, SCX, COL1A1 and OCN in woven scaffolds. After cell permeabilization with 0.1% Triton X-100/PBS solution, for 20 min at RT, and washing with PBS, samples were blocked with RTU Normal Horse Serum for 40 min. Then, cells were incubated overnight with primary antibodies against YAP/TAZ, TNMD, SCX and COL1A1, and diluted in antibody diluent with background reducing components at 4°C . Samples

were then rinsed in 0.1% Triton X100/PBS solution followed by incubation for 1 h at RT with the respective Alexa fluor 488 secondary antibodies. Samples were stained with DAPI for 15 min and with phalloidin for 30 min for cell nuclei and cytoskeleton labelling, respectively. Immunolabeled samples were analyzed by confocal laser scanning microscopy (Leica TCS SP8, Microsystems, Wetzlar, Germany).

2.7.5. Cytoskeleton organization. Cell alignment was assessed following a similar method to the one previously described for analyzing PCL fiber alignment. Using the directionality plugin from ImageJ, directionality histograms were generated to translate the amount of structures in the image along an angle of orientation (-90 – 90°). Histograms of each condition ($n = 5$) were fitted with a Gaussian function using Origin Lab software. To assess actin filament organization, the height and FWHM of the peaks from each condition were evaluated.

2.7.6. YAP/TAZ and mean fluorescence level quantification. The ratio of nuclear/cytoplasmatic YAP/TAZ in cells cultured for 11 days was assessed by calculating the fluorescence intensity of the nuclei and of the respective cytoplasm from confocal microscopy images ($n > 6$). For this purpose, each image was pre-processed with ImageJ to remove outliers, followed by image segmentation using MATLAB software. Finally, the nuclear/cytoplasmatic YAP/TAZ ratio was obtained by dividing the intensity of the segmented nuclei by the intensity of the segmented cytoplasm. The expression levels of SCX and TNMD were assessed by calculating the mean fluorescence intensity of obtained confocal images ($n > 5$) at the indicated time points using Image J. To calculate the mean intensity of each protein marker, images were thresholded to separate the signal from the background and then the mean fluorescence values were calculated and normalized by the total signal area.

2.8. Statistical analysis

Statistical analysis of data was performed using GraphPad PRISM version 6.01. One-way analysis of variance (ANOVA) was performed in normal distributed populations followed by the Tukey *post hoc* test for multiple comparisons, whereas the Kruskal–Wallis non-parametric test was performed otherwise. The unpaired *t* test was performed to compare two normal distributed populations. The statistical significance was set to $p < 0.05$ and results are presented as mean \pm standard deviation.

3. Results and discussion

3.1. Production and characterization of magnetic nanoparticles

Fig. 1A illustrates the production process of the hybrid magnetic nanoparticles. Besides acting as reinforcement nanofillers for electrospun fibers,⁴² CNCs were used as nucleating sites to anchor and pseudo-disperse iron oxide MNPs through *in situ* co-precipitation of Fe^{2+} and Fe^{3+} .⁴³ To ensure their chemical and colloidal stability while improving their interfacial compatibility with the polymeric matrix, the surface of

MNP@CNC was first modified with thin layers of PDA (PDA-NP) that were then used as convenient means for further grafting 1-DT (DT-NP) through Michael's addition reaction. Due to the hydrophilic nature of PDA and its excellent chelation properties towards metallic ions, this strategy results in a robust coating⁴⁴ that ensures the steric stabilization of MNP@CNCs, thereby preventing particle aggregation in aqueous suspensions. On the other hand, subsequent functionalization of the PDA coating with the long chain aliphatic thiol^{45,46} increases the hydrophobicity of MNP@CNC, improving their dispersion in the non-polar or polar aprotic organic solvents commonly used for electrospinning PCL,⁴⁷ as well as their interfacial compatibility with the hydrophobic PCL polymer matrix to maximize the nanofiller reinforcement potential in the nanocomposite scaffolds.

AFM and STEM images of the produced nanoparticles are shown in Fig. 1B. CNCs presented the characteristic rod-shape⁴⁸ with 216.5 ± 71.4 nm length and 4.3 ± 1.7 nm height, while MNP@CNC exhibited spherical MNPs anchored on the CNCs' surface. MNP@CNC morphology is maintained after the coating processes and the final DT-NP appear well-dispersed and individualized with the coating involving both the CNCs and anchored MNPs. FTIR spectra of the produced nanoparticles are shown in Fig. 1C and Fig. S1 (see the ESI†). MNP@CNC spectra exhibited characteristic peaks of cellulose and iron oxide confirming the formation of the hybrid nanoparticles (see the ESI, Fig. S1†). The characteristic bands of PDA in PDA-NP at 1612, 1501 and at 1280 cm^{-1} (Fig. 1Cii) assigned to the N–H bending in the primary amine, C=C phenylic stretching and stretching of the phenolic OH (C–O), respectively, confirm the PDA coating, whereas 1-DT grafting was confirmed by the appearance of two new well defined peaks at 2920 and 2848 cm^{-1} in the DT-NP spectra (Fig. 1Ci), corresponding to the CH_2 stretching of the 1-DT long alkyl chain.^{49,50} The iron oxide MNPs were identified by X-ray diffraction (XRD) as magnetite (Fe_3O_4) with a crystallite size of 7.4 ± 0.5 nm (see the ESI, Fig. S2 and Table S1†), and the content of the magnetic material adsorbed onto the CNCs was estimated to be 32.4 wt% by thermogravimetric analysis (TGA; see the ESI, Fig. S3†). Finally, the magnetic properties of the nanoparticles were assessed through VSM studies (Fig. 1D). The low coercivity and the absence of distinct hysteresis loops and of remanence confirm the superparamagnetic behavior of all the nanoparticles. The MNP@CNC have a magnetization of saturation (M_s) of 18.18 emu g^{-1} , lower than that of similar hybrid MNP@CNC⁴³ but consistent with their comparatively lower magnetic content (32.4 wt% vs. $\sim 50\text{ wt}\%$ ⁴³) and MNP diameter (7.4 ± 0.5 nm vs. 18–30 nm (ref. 43)). After PDA coating and 1-DT grafting, the M_s of hybrid nanoparticles decreased to 8.43 emu g^{-1} , reflecting the respective decrease in the magnetic material mass fraction of the final nanoparticles.

3.2. Production and characterization of electrospun fibrous constructs

By applying our previously proposed electrospinning system to produce 3D scaffolds with tendon mimetic fibrous hierarchical

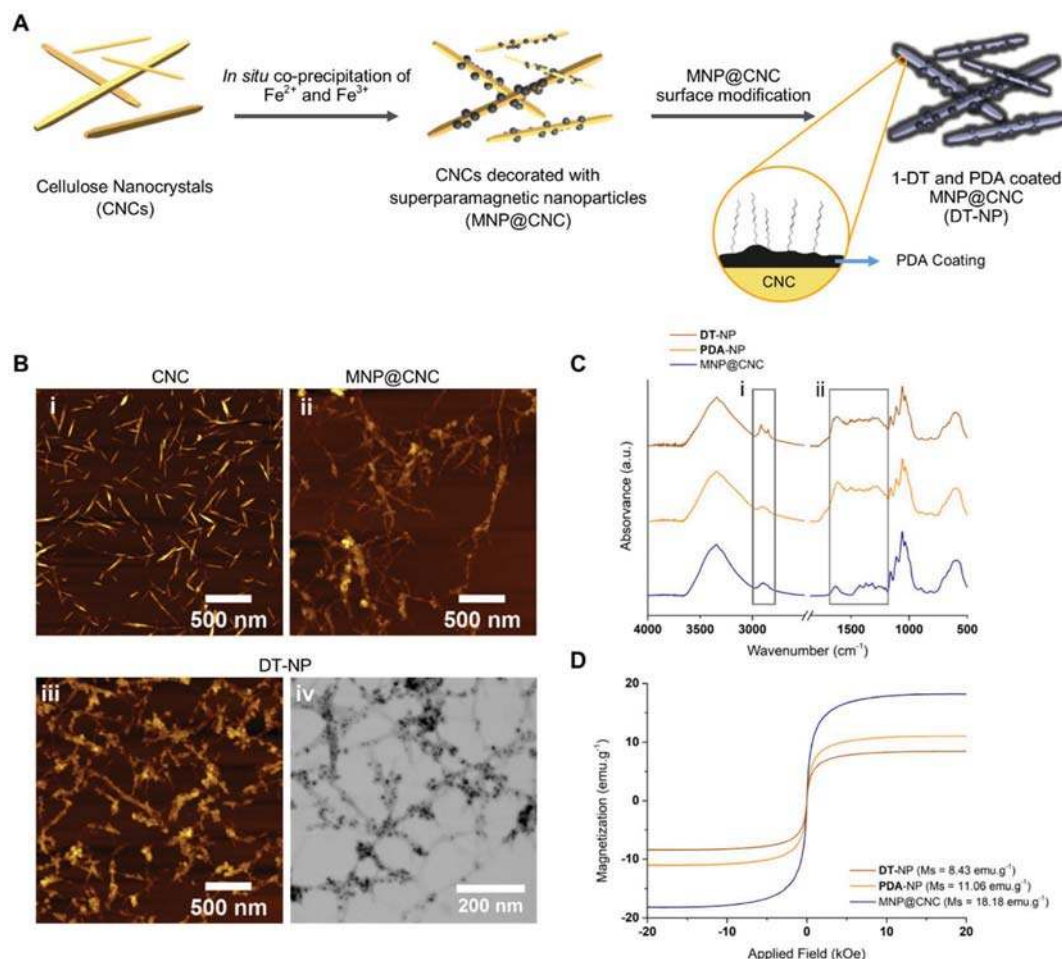


Fig. 1 Production and characterization of the hybrid magnetic nanoparticles. (A) Schematic illustrating the main steps involved in the production process. (B) AFM images of CNCs (i), MNP@CNCs (ii) and of DT-NP (iii); STEM image of DT-NP (iv). (C) FTIR spectra of MNP@CNC, PDA-NP and DT-NP. Grey squares (i and ii) represent regions of the spectra in which characteristic peaks of the different species can be identified. (D) Magnetic hysteresis curves of MNP@CNC, PDA-NP and DT-NP. Magnetization of saturation (M_s) of each sample is shown next to the respective label.

architecture,¹³ continuous and aligned fiber threads were first fabricated by jetting the spinning solution onto the surface of a grounded liquid bath, from which the resulting fibers were collected by using a roller at constant speed (Fig. 2A). PCL electrospun threads were reinforced with different nanofiller contents (0–7.5 wt% DT-NP, PCL/DT-NP) aiming to simultaneously maximize their mechanical and magnetic properties. The produced threads were then twisted into yarns (12 threads each) thus mimicking the hierarchical fibrous organization of native tendon fascicles.¹³ Fig. 2C shows the influence of the nanofiller content on the thread morphology. An overall increase in both thread and fiber diameters with the increase of the nanofiller content (see the ESI, Fig. S4†) was observed. Although the quality of the nanoparticle dispersion could not be evaluated in detail at the higher nanofiller concentrations due to their high fiber thickness that restricts transparency in STEM analysis, at 2.5 wt% there was a homogeneous dispersion of DT-NP within the core of the electrospun fibers without showing apparent aggregates (Fig. 2B). Moreover,

increasing the nanofiller content did not impair the spinning process up to 7.5 wt%, although at this higher DT-NP concentration it was quite unstable, probably due to the higher viscosity of the spin dope solution that prevents the formation of a uniform jet.⁵¹ The possible occurrence of some nanoparticle aggregation at 7.5 wt% DT-NP cannot be excluded since it leads to brittle threads with visually variable diameters along their length ($218.1 \pm 106.7 \mu\text{m}$; see the ESI, Fig. S4†). Apart from PCL/DT-NP7.5 solutions, all formulations generated threads of consistent diameters and with smooth, bead-free fibers (Fig. 2C), and therefore the PCL/DT-NP7.5 formulation was excluded from further characterization. Fig. 2D shows SEM characterization images of PCL/DT-NP5 threads illustrating the influence of the take-up speed on their morphology. An increase in the take-up speed leads not only to a higher anisotropic alignment of the fibers but also to thinner threads. Thus, depending on the nanofiller content and take up speed, thread diameters varied from $44.9 \pm 8.3 \mu\text{m}$ for bare PCL taken at 0.73 m s^{-1} , up to $184.9 \pm 39.1 \mu\text{m}$ for PCL/DT-NP5 taken at

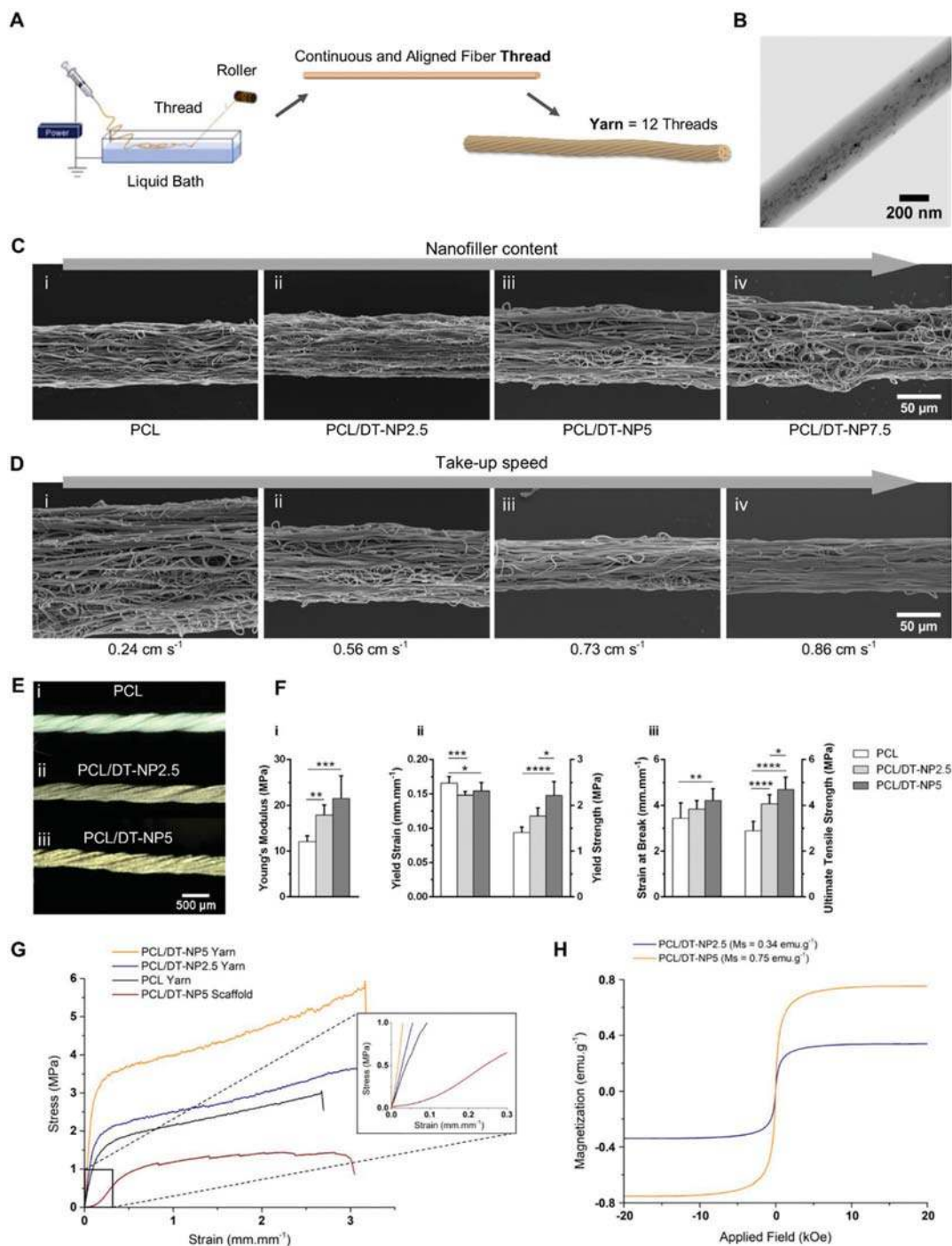


Fig. 2 Fabrication and characterization of continuous and aligned electrospun fiber threads and yarns. (A) Schematic illustrating the main steps involved in the fabrication of these fibrous constructs from the electrospinning setup up to the yarns. (B) STEM image showing the dispersion of hybrid magnetic nanoparticles within PCL/DT-NP2.5 fibers. (C) SEM images of PCL threads fabricated with different nanofiller contents (0–7.5 wt%) under the same spinning conditions. (D) SEM images of PCL/DT-NP5 threads fabricated with increasing take-up speed (0.24–0.86 cm s^{-1}). (E) Optical microscopy images of the yarns. (F) Mechanical properties of electrospun yarns of increasing nanofiller content ($*p \leq 0.05$, $**p \leq 0.01$, $***p \leq 0.001$, $****p \leq 0.0001$). (G) Representative stress–strain curves of the fabricated yarns and 3D scaffolds with an inset showing the behavior at low strains. (H) Hysteresis curves of PCL/DT-NP2.5 and PCL/DT-NP5 yarns. Magnetization of saturation (M_s) of each sample is shown next to the respective label.

0.24 cm s^{-1} . Similar trends were observed for the diameter of the fibers composing the threads that varied between 1.1 ± 0.3 and $0.7 \pm 0.3 \mu\text{m}$, 1.2 ± 0.3 and $0.7 \pm 0.3 \mu\text{m}$, and 1.9 ± 0.4 and

$1.3 \pm 0.4 \mu\text{m}$ for threads reinforced with 0, 2.5 and 5 wt% of DT-NP, respectively (see the ESI, Fig. S5†). Regardless of the nanofiller content, 0.73 cm s^{-1} take-up speed resulted in the

thinnest threads, whereas increasing the speed to 0.86 cm s^{-1} leads to an increase in the thread diameter, which also made the threads more prone to breaking (lower processability). In general, the fabricated threads were composed of fibers with diameters within the range of those reported in other electrospun scaffolds based on PCL for tendon TE ($\sim 400 \text{ nm}$ to over $1 \mu\text{m}$ in diameter).^{52–56} In terms of correspondence with the hierarchy of the tendon ECM fibrous structure, the thread matched the diameter of fascicles ($150\text{--}1000 \mu\text{m}$)^{3,4} whereas the diameter of the fibers is within the range of collagen fibers ($1\text{--}20 \mu\text{m}$)^{3,4} (see the ESI, Table S2†). Interestingly, it has been suggested that electrospun scaffolds composed of microfibers ($\sim 1.40 \mu\text{m}$ to $\sim 1.80 \mu\text{m}$), such as those obtained here from PCL/DT-NP5, rather than nanofibers ($\sim 300 \text{ nm}$ to $\sim 650 \text{ nm}$) are preferable to maintain the tenogenic phenotype of tenocytes.^{57,58} It was suggested that while nano-sized fibers recapitulate the early stages of tissue repair, characterized by the deposition of disorganized temporary collagen fibers and scar tissue formation,⁵⁸ micron sized fibers resemble a later remodeling stage in which the collagen fibers display a closer diameter and organization to those of healthy tendons.⁵⁷ Moreover, cells seeded onto microfiber scaffolds have shown an upregulation of tenogenic markers and promote higher cell alignment and elongation in comparison with nanofibrous scaffolds.^{57,58}

The influence of the take-up speed on fiber alignment was evaluated in SEM images of PCL/DT-NP5 threads, from which directionality histograms of the respective fibers were calculated and the difference between conditions was quantified by fitting the respective peaks with a Gaussian function (see the ESI, Fig. S6†). An increase in the take-up speed resulted in both higher and thinner peaks, indicating an increase in the anisotropic alignment of fibers. Since threads taken-up at 0.73 cm s^{-1} exhibited the best combination of processability and degree of fiber alignment, they were produced applying these parameters and then assembled into yarns with diameters of $346.93 \pm 31.08 \mu\text{m}$, $313.08 \pm 33.48 \mu\text{m}$ and $326.45 \pm 33.09 \mu\text{m}$ for 0, 2.5 and 5 wt% DT-NP loading, respectively (Fig. 2E). The impact of the nanofiller content on the mechanical properties of the yarns was evaluated (Fig. 2Fi–iii). Tensile tests demonstrate that incorporation of DT-NP into the fibrous constructs had a significant and positive impact on their mechanical properties, confirming the reinforcement effect of the hybrid nanoparticles (see the ESI, Table S3†). Their Young's modulus increased 78% (from 12.10 ± 1.26 to $21.55 \pm 4.91 \text{ MPa}$, Fig. 2Fi), the yield strength increased 58% (from 1.41 ± 0.12 to $2.22 \pm 0.30 \text{ MPa}$, Fig. 2Fii) and the ultimate tensile strength increased 62% (from 2.90 ± 0.41 to $4.70 \pm 0.53 \text{ MPa}$, Fig. 2Fiii) in PCL/DT-NP5 threads in comparison with bare PCL ones. The Young's modulus and ultimate tensile strength of PCL/DT-NP5 yarns are within the lower range of native tendon tensile properties ($20\text{--}1200 \text{ MPa}$ and $5\text{--}100 \text{ MPa}$, respectively).⁵⁹ Their yield strain, although just $0.15 \pm 0.01 \text{ mm mm}^{-1}$ (Fig. 2Fii), is adequate for tendon TE applications given that the native tissue physiological range is 4% strain.⁶ The characteristic stress–strain curves of the bare PCL and

reinforced PCL constructs are shown in Fig. 2G. Although all the tested formulations show a non-linear profile with linear and yield regions, as expected they do not show a toe region, an hallmark of tendon's biomechanical behavior, which reflects their strain-stiffening character at low strains and is ascribed to the uncrimping of collagen fibers in native tissues.⁶ As we have previously shown, this feature can be recapitulated by weaving the yarns into 3D woven scaffolds.¹³ To demonstrate this effect, PCL/DT-NP5 yarns were assembled into woven scaffolds. As shown in Fig. 2G, the stress–strain curves of higher hierarchical woven scaffolds display the toe region that is lacking in the remaining curves, replicating the characteristic triphasic biomechanical behavior of native tendons.

The magnetic properties of reinforced yarns were also evaluated (Fig. 2H) and, as expected, increasing the content of the magnetic material in the constructs leads to an increase in their M_s from 0.34 to 0.75 emu g^{-1} . Similarly to the observed for DT-NP, the low coercivity, and the absence of remanence magnetization and distinct hysteresis loops confirm the superparamagnetic behavior of the nanocomposite scaffold biomaterial. These M_s values, particularly of PCL/DT-NP5 yarns, are of the same order of other previously developed electrospun scaffolds comprising similar amounts of superparamagnetic iron oxide nanoparticles.^{31,33} Moreover, these and other scaffolds with similar M_s values demonstrated to be able to influence cellular responses when combined with magnetic actuation.^{31,33–35}

Overall, PCL/DT-NP5 nanocomposites displayed the highest mechanical properties and M_s while maintaining a tendon mimetic fibrous architecture. Therefore, this formulation was selected to evaluate the biological performance of the system.

3.3. Biological performance of electrospun scaffolds

The biologic performance of the developed magnetic system was firstly evaluated using yarns, synthetic mimics of tendon fascicles, as representative units of the 3D woven scaffolds. To evaluate the potential of magnetically actuated scaffolds for tendon TE, after this first assessment the results were also validated on the 3D woven scaffolds. For these biological studies, hASCs were cultured on the constructs for up to 21 days, with and without magneto-mechanical stimulation (Fig. 3A).

3.3.1. Cell morphology and metabolic activity. Metabolic activity of seeded hASCs was assessed through MTS assay (Fig. 3E). Cells remained viable over time showing a significant increase in metabolic activity and cell density between (Fig. 3B) day 11 and day 21 for both culture conditions. No significant differences were observed between the metabolic activity of cells cultured under magnetic stimulation and those in static culture, suggesting that the mechanical loading *via* magnetic actuation does not affect this cell parameter.

Cell morphology and organization were evaluated over time by quantifying the development of uniaxial alignment of the actin filaments (Fig. 3B). As expected, cells cultured under both conditions, static and magnetic stimulated, exhibit high

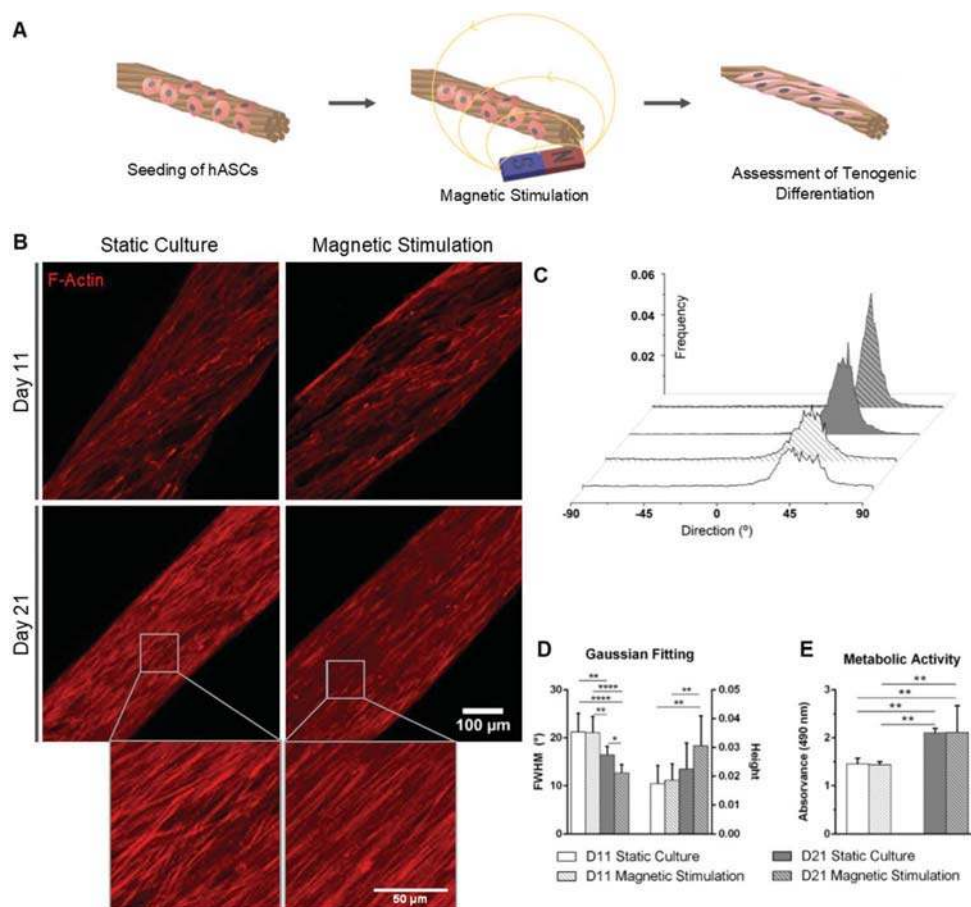


Fig. 3 Morphometric analysis and metabolic activity of hASCs seeded onto PCL/DT-NP5 yarns. (A) Schematic illustrating the main steps involved in the assessment of the biological performance of electrospun constructs. hASCs were cultured on the electrospun yarns under static or magnetic stimulation conditions for up to 21 days. (B) Confocal microscopy images of the cytoskeleton of hASCs (red: phalloidin) cultured on PCL/DT-NP5, for 11 and 21 days (higher magnification view in the insets) and (C) the respective directionality spectra. (D) Comparison between the dimensions of the directionality peaks (FWHM and height) obtained after Gaussian fitting of the spectra from each condition ($n = 5$) (** $p \leq 0.01$, **** $p \leq 0.0001$). (E) Metabolic activity of hASCs assessed by MTS assay (** $p \leq 0.01$).

anisotropic alignment along the direction of the yarn fibers, induced by the known contact guidance mechanisms.^{60,61} Irrespective of the stimulation regime to which cells were subjected, the aligned topography set by the construct fibers promotes a tenocyte-like morphology which is characterized by an elongated cell shape.^{4,62} After 21 days of culture, a thick, well-aligned layer of cells can be observed on the yarn surface indicating that cell organization is maintained during proliferation. The degree of cytoskeleton alignment was quantified by directionality analysis of F-actin images acquired for each culture condition (Fig. 3C). Similarly to the procedures performed to assess fiber alignment within electrospun threads, the resultant histograms were fitted to a Gaussian function (Fig. 3D). Overall, although there is a preferential direction of alignment for all the tested conditions, histograms of cells cultured under magnetic stimulation for 21 days show monomodal directionality peaks with a significantly lower FWHM accompanied by a higher peak height trend. These results suggest that, compared with the static culture conditions, the

mechanical stimulation of cells, herein performed through remote magnetic actuation of the constructs, enhances cell uniaxial alignment and elongation along the longitudinal direction of the fibers.

3.3.2. Response to the magneto-mechanical stimulus. Cell cytoskeleton organization is strongly dependent on how cells perceive external mechanical cues. In response to mechanical input, such as ECM stiffness, geometry or mechanical loading, cells can adapt their behavior in terms of proliferation, differentiation or tissue phenotype maintenance through mechanotransduction.⁶³ This process relies on the physical connection provided by focal adhesions between the ECM and the F-actin cytoskeleton of cells.⁶⁴ Thus, external physical signals such as deformation of the culture substrate can be explored to directly influence key cell functions.¹⁸ One of the suggested mediators between the mechanical stimulus perceived by the cytoskeleton and the corresponding cell response are two transcriptional activators, YAP (Yes-associated protein) and TAZ (transcriptional coactivator with PDZ binding motif).^{65–68} YAP/TAZ

are predominantly cytoplasmic, though upon activation, they shuttle from the cytoplasm to the nucleus where they regulate gene expression.^{65–67} Importantly, an increase in nuclear YAP/TAZ is indicative of tension of the cytoskeleton which is likely caused by its adjustment to the external physical stimulus,^{18,69} a common phenomenon in cell spreading and proliferation,⁶⁷ but has also been correlated with stem cell differentiation.⁷⁰

Thus, we evaluated the expression of YAP/TAZ in hASCs cultured for both 11 and 21 days (Fig. 4) as an indirect test to prove if the developed magnetic scaffolds can deliver mechanical stimuli to seeded cells upon remote magnetic actuation and induce the mechanotransduction mechanism that can act as promoters for tenogenic commitment. In fact, it has been previously estimated that, in a typical cell culture stimulation experiment applying magnetic fields as low as 1.5 mT on alginate-based magnetic scaffolds incorporating 1.2 wt% MNPs, the force acting on an endothelial cell is about 1 pN.²⁸ The order of magnitude of this force is above the reported threshold of 0.2 pN required to induce cellular mechanotransduction⁷¹ and can easily be increased by increasing the strength of applied magnetic fields. Our hypothesis is that the applied magnetic field (around 300 mT) acting on the mag-

netic nanoparticles as remote actuators can induce small deformations on the respective nanocomposite fibers. As a result, the cell cytoskeleton is subjected to increasing tension, thus transmitting more strain to the nucleus and activating YAP/TAZ shuttling⁶⁵ (Fig. 4B). Immunofluorescence images of hASCs cultured under both conditions for 11 days (Fig. 4A) clearly display expression of predominant nuclear YAP/TAZ. The fact that the constructs were able to induce YAP/TAZ activation under both non-stimulating and stimulation conditions demonstrates that their aligned topography is sufficient to induce enough cell polarization and cytoskeleton tension to trigger this effect, as previously shown in other anisotropic systems.^{65,66} Remarkably, results indicate that the nuclear to cytoplasmic YAP/TAZ ratio in stimulated cells at day 11 is significantly higher than that of cells cultured in static culture (Fig. 4C), suggesting an effective transmission of the mechanical load signals from the scaffold to the cell cytoskeleton.⁶⁹ Note that we have previously shown that YAP/TAZ expression remained unaltered when similar magnetic stimuli were applied in tendon derived cells cultured on nonmagnetic materials,⁷² further supporting the hypothesis that in the present system the delivered stimuli have a physical loading

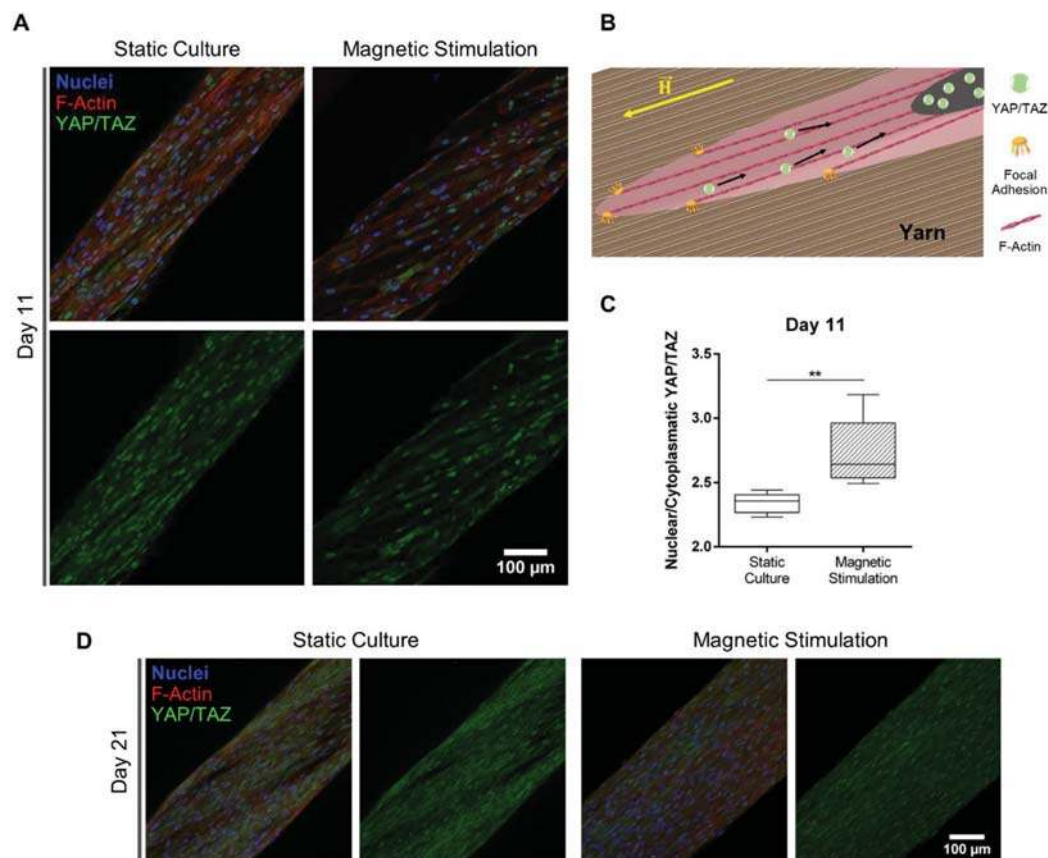


Fig. 4 Analysis of the mechanotransduction mechanism resultant of the magneto-mechanical stimulation of hASCs. (A) Confocal microscopy images of hASCs cultured on PCL/DT-NP5 yarns for 11 days under static and magnetic stimulated conditions. (B) Schematic illustrating the shuttling of nuclear/cytoplasmic YAP/TAZ in response to substrate deformations caused by the applied magnetic field (H). (C) Ratio of nuclear/cytoplasmic YAP/TAZ in hASCs cultured for 11 days (** $p \leq 0.01$). (D) Confocal microscopy images of hASCs cultured on PCL/DT-NP5 yarns for 21 days under static and magnetic stimulated conditions. Nuclei are stained in blue (DAPI), actin filaments in red (phalloidin) and YAP/TAZ in green.

nature. In contrast, immunofluorescence images of hASCs cultured for 21 days (Fig. 4D) showed predominantly cytoplasmic YAP/TAZ, most likely due to cell crowding and decrease in proliferation.⁶⁷ Overall, magneto-mechanical stimulation of cells was capable of early activating YAP/TAZ, suggesting an effective transmission of mechanical stimulus that can be correlated with higher cytoskeleton tension resulting from the enhanced cell polarization observed under this culture condition (Fig. 3).

3.3.3. Gene expression. As a first assessment on the impact of magneto-mechanical stimulation on cell tenogenic commitment, real time reverse transcription polymerase chain reaction (RT-PCR) was applied to evaluate the gene expression profile of cultured cells, particularly focusing on a panel of tendon related markers including tenomodulin (TNMD), type I collagen (COL1A1), decorin (DCN), tenascin-C (TNC), type III collagen (COL3A1) and scleraxis (SCX).^{73,74} RT-PCR results suggest that cells cultured on PCL/DT-NP5 under both static and magnetic conditions present upregulated expression of tendon-related markers after 11 days of culture (Fig. 5i), confirming that the yarns topographical and architectural cues are themselves strong inducers of hASC tenogenic commitment, as expected.¹³ Remarkably, magneto-mechanical stimulation of hASCs leads to higher expression of SCX and TNMD, two well recognized tendon markers. Scleraxis is responsible for the promotion and consequent regulation of the expression of TNMD in mature tenocytes,⁷⁵ as well as for directing mesenchymal stem cell differentiation towards the tenogenic lineage in response to mechanical stimulus and suppressing commitment towards other phenotypes.⁷⁶ Tenomodulin is a transmembrane glycoprotein expressed mainly in tenocytes that regulates their proliferation and is involved in the calibration of collagen fibrils.⁷⁷ On the other hand, the expression of non-tendon-related markers was lower in cells cultured under magneto-mechanical stimulation, particularly RUNX2, an osteogenic-related gene that was downregulated.⁷⁸ Overall, these results indicate that magneto-mechanical stimulation of hASCs cultured on PCL/DT-NP5 yarns tends to increase the gene expression of markers that are crucial for inducing the tenogenic commitment of hASCs and regulating the tenocyte phenotype, while decreasing the expression of genes related to other lineages.

Tendon ECM remodeling by the activity of matrix metalloproteinases (MMPs) and MMP tissue inhibitors (TIMPs) is known to be promoted by mechanical stimuli.⁷⁹ MMPs and TIMPs are central in reparative processes and the balance between their activities is essential for tissue homeostasis in healthy tendons.^{7,80} Therefore, the expression of MMPs, namely 1, 2 and 3, and TIMP1 genes was also assessed in constructs cultured under static and magnetic stimulation conditions. Results (Fig. 5ii) show that cells cultured under magneto-mechanical stimulation tend to express higher levels of MMPs and TIMP1 in comparison with those in static culture. This behavior is in agreement with recent studies showing that the matrix remodeling potential of tendon-derived cells is influenced by the structure of the extracellular

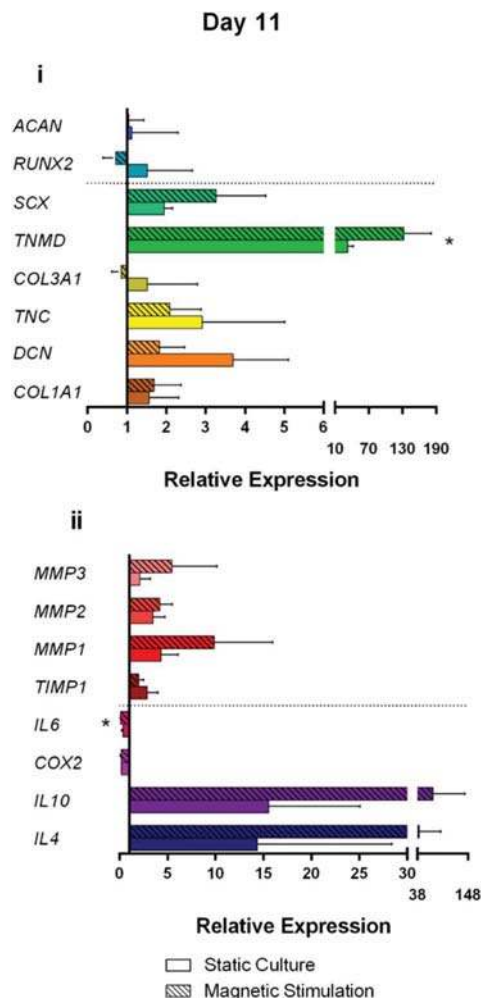


Fig. 5 Effect of magneto-mechanical stimulation on the gene expression of hASCs. Real time RT-PCR analysis of tenogenic (COL1A1, type I collagen; DCN, decorin; TNC, tenascin; COL3A1, type III collagen; TNMD, tenomodulin; SCX, scleraxis), chondrogenic (ACAN, aggrecan) and osteogenic (RUNX2) gene expression (i), as well as anti-inflammatory (IL-4 and IL-10) and pro-inflammatory (IL-6 and COX2) cytokines, and matrix metalloproteinases (MMP) and MMP tissue inhibitor (TIMP) (ii) of hASCs cultured on PCL/DT-NP5 yarns for 11 days under static and magnetic stimulated conditions (* $p < 0.05$).

environment, with anisotropic substrates improving their remodeling capacity in comparison with isotropic ones.⁸¹ Moreover, higher expression levels of MMP and TIMP were observed in substrates that presented increased anisotropic organization and were mechanically stimulated, indicating an enhanced remodeling response in comparison with non-stimulated substrates.⁸¹ Therefore, our results suggest that cells cultured under magneto-mechanical stimulation present enhanced remodeling potential in comparison with those in static culture.

Although biomimetic scaffolds can be an effective strategy to promote tissue regeneration, their implantation will most likely lead to an host inflammatory response at the injury site that can compromise the healing process if not resolved in a

controlled manner.³¹ Modulation of the inflammatory response through biomaterial design approaches or stimulatory strategies might therefore contribute to the improvement of the regenerative outcomes of TE strategies. Immunoregenerative biomaterials capable of inducing the polarization of macrophages (directly or indirectly by modulating the secretome of stem cells) from inflammatory (M1) to anti-inflammatory or pro-regenerative (M2) phenotypes have been quite successful^{82,83} and include design strategies based

on aligned nano- and micro-patterned surfaces.^{84,85} Thus, the expression of genes related to the inflammatory secretome of stem cells cultured on PCL/DT-NP5 yarns under static and magnetic conditions, namely the expression of both pro (COX2 and IL6)⁸⁶ and anti-inflammatory markers (IL4 and IL10),^{87,88} was also assessed. Results (Fig. 5ii) show an upregulation of anti-inflammatory and downregulation of pro-inflammatory markers in cells cultured under both conditions. Moreover, magneto-mechanical stimulation of hASCs leads to a higher

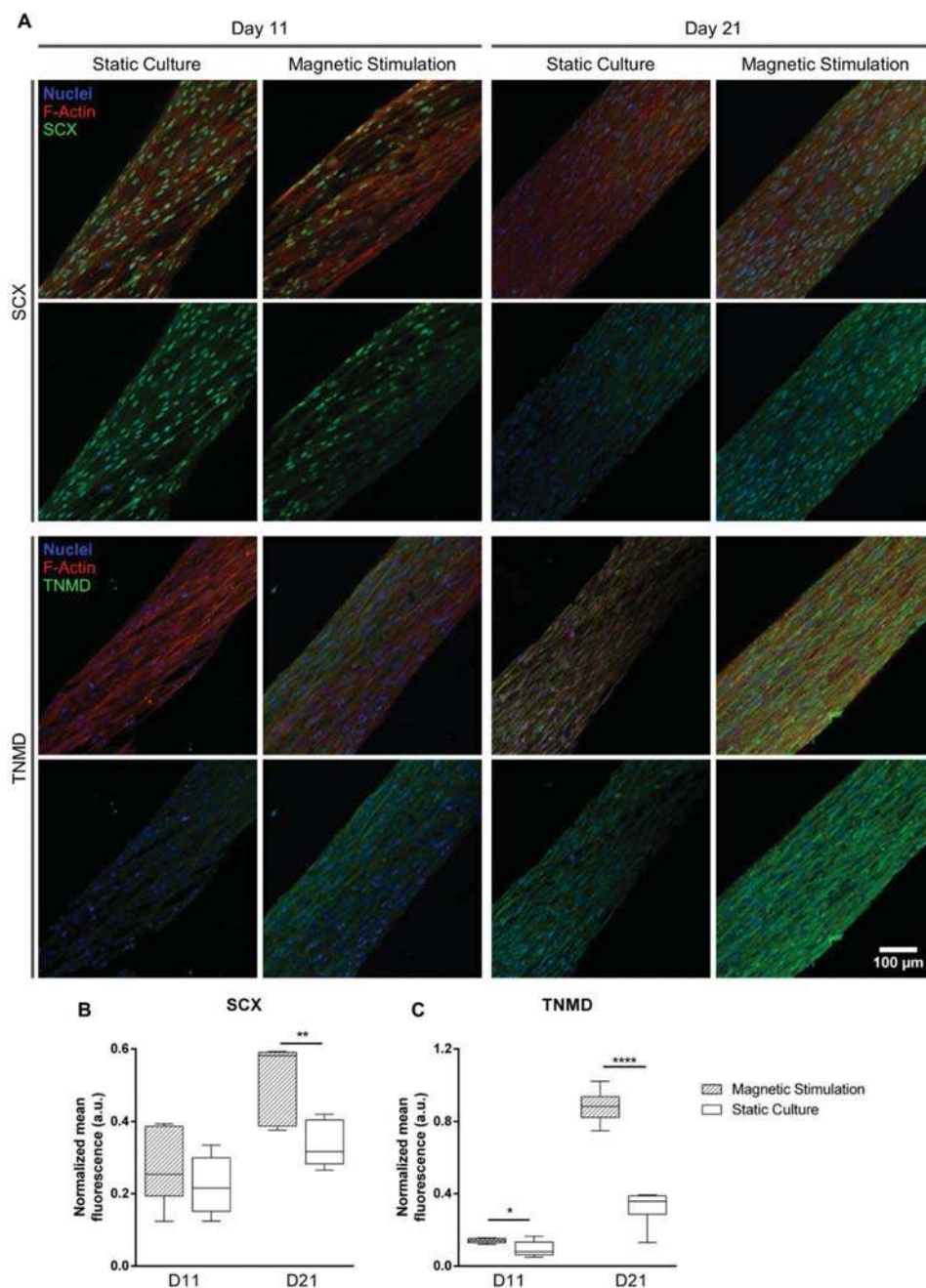


Fig. 6 Expression of tendon-related markers. Confocal microscopy images (A) and normalized mean fluorescence intensity quantification of SCX (B) and TNMD (C) expressed by hASCs cultured on PCL/DT-NP5 yarns for 11 and 21 days under static and magnetic stimulated conditions (scale bar 100 μ m). Nuclei are stained in blue (DAPI), actin filaments in red (phalloidin) and SCX/TNMD in green (* $p \leq 0.05$, ** $p \leq 0.01$ and **** $p \leq 0.0001$).

expression of anti-inflammatory markers and a significantly lower expression of IL-6. These results suggest that the effects stemming from yarns' aligned topography combined with remote magneto-mechanical stimulation have a positive impact on the immunomodulatory behavior of hASCs that

might potentially promote subsequent pro-regenerative macrophage phenotypes. Interestingly, our results on the impact of the magneto-mechanical stimuli over the activation of mechanotransduction mechanisms and gene expression are in good agreement with recent reports identifying YAP/TAZ sig-

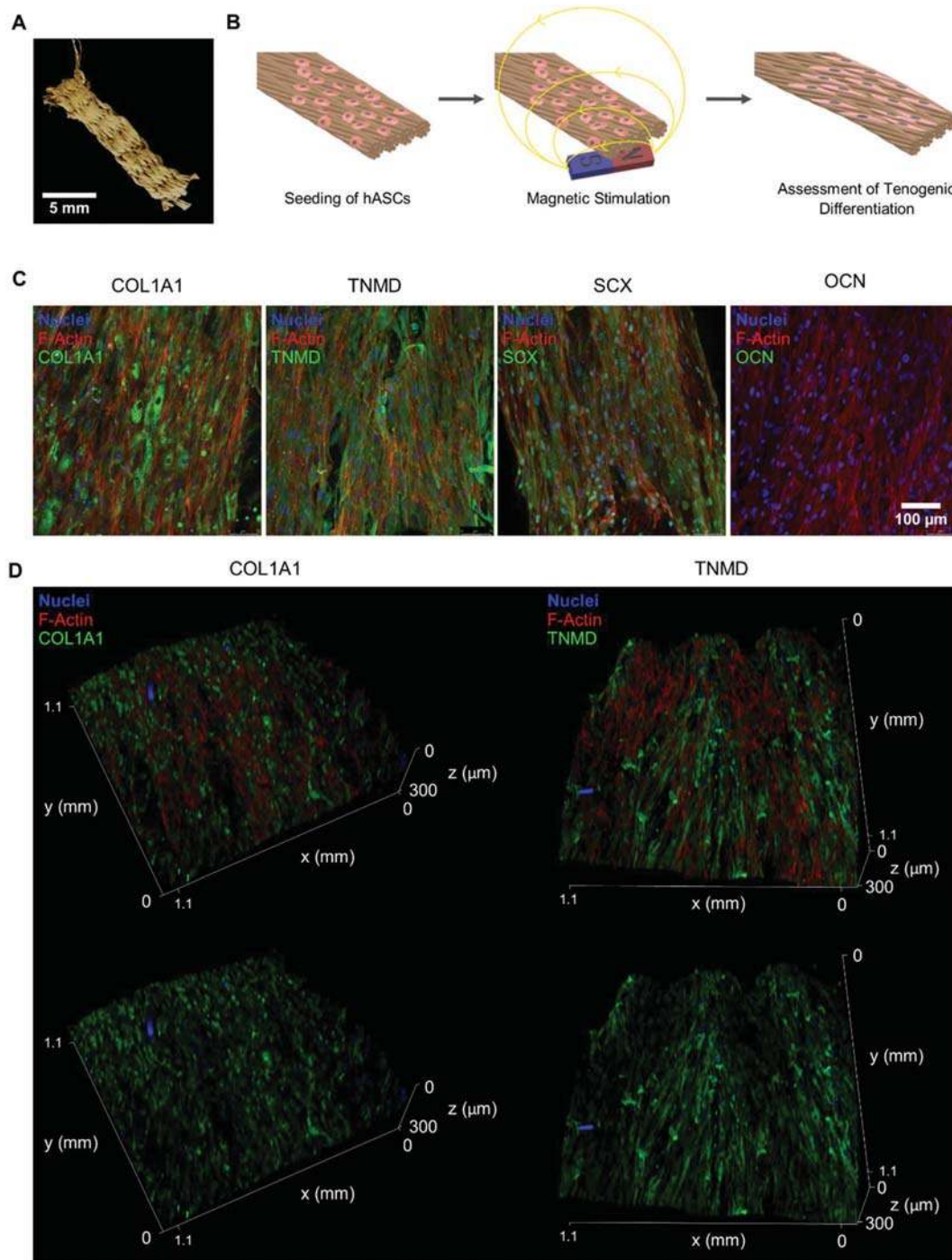


Fig. 7 Expression of tendon and non-tendon related protein markers by hASCs cultured on 3D scaffolds. (A) Optical microscopy images of a PCL/DT-NP5 woven scaffold. (B) Schematic illustrating the main steps involved in the assessment of the biological performance of the scaffolds. (C) Confocal microscopy images of tendon and non-tendon related protein markers expressed by hASCs cultured on the scaffolds and their (D) 3D reconstructions. Nuclei are stained in blue (DAPI), actin filaments in red (phalloidin) and COL1A1/TNMD/SCX/OCN in green.

naling as required pathways through which aligned fibers stimulate the immunomodulatory function of hASCs, whose paracrine secretions were capable of inducing M2 phenotypic changes in macrophages.⁶⁶ Moreover, although not studied here, it has been recently demonstrated that magneto-mechanical stimulation of macrophages through magnetic responsive materials has itself a positive effect on their M2 polarization.³¹ Altogether, these results suggest that magnetic actuation of implanted PCL/DT-NP5 constructs might not only promote tenogenic commitment of stem cells but can also contribute to positively modulating the inflammatory response of the native tissue, thus preventing chronic inflammation and minimizing scar tissue formation.

3.3.4. Expression of tendon-related markers and production of the tendon-like ECM. Immunocytochemistry analysis was performed to further assess at the protein expression level the presence of tenogenic-related markers at 11 and 21 days of culture (Fig. 6). In general, hASCs cultured under static and magnetic stimulating conditions express both SCX and TNMD at the two time points studied, showing a relatively decreased nuclear localization of SCX and an increase in the expression of TNMD from day 11 to day 21, in agreement with the role of SCX as a transcription factor for TNMD.⁷⁵ Although the expression profile of SCX at day 11 is similar under both conditions, cells cultured under magneto-mechanical stimulation express higher levels of the downstream TNMD, suggesting an earlier and/or more efficient activation of SCX under this condition. At the 21st day, cells under magneto-mechanical stimulation express higher levels of both SCX and TNMD in comparison with those under static conditions, which is indicative of a more sustained commitment of the cell toward tenogenic lineage.^{77,89} Remarkably, SCX is known to be required for the mechanically stimulated tenogenesis of stem cells and has recently been suggested to facilitate mechanosensing in adult tenocytes by regulating the expression of several mechanosensitive focal adhesion proteins.⁹⁰

Finally, PCL/DT-NP5 yarns were woven into higher hierarchical 3D scaffolds (Fig. 7A) in order to evaluate whether these constructs could perform similarly to their representative miniaturized yarn units. For this purpose, hASCs were cultured on the scaffolds under magnetic stimulation for 21 days (Fig. 7B) and immunocytochemistry analysis was performed to investigate the expression of tendon and non-tendon related protein markers (Fig. 7C). Results indicate high expression levels of TNMD and SCX, similarly to the behavior observed on the yarns (Fig. 6). Additionally, the secretion of considerable amounts of COL1A1, showing apparent signs of fibrillation and following the cell aligned patterns, could also be observed (Fig. 7D). On the other hand, given that several magnetic scaffold systems combined with magnetic stimuli have been proposed for bone regeneration,^{32,33,91} the expression of osteocalcin (OCN), a specific marker for osteogenic differentiation,⁹² was also investigated to assess the potential phenotypic drift of hASCs. As shown in Fig. 7C, the deposition of OCN in magnetically actuated scaffolds is negligible, indicating that

osteogenic differentiation of hASCs is unlikely to be triggered by magneto-mechanical stimulation in our system. Overall, these results demonstrate that the 3D tendon mimetic hierarchical architecture and topography of the proposed magnetic responsive scaffolds in combination with magneto-mechanical stimulation can synergistically boost the tenogenic commitment of stem cells by steering mechanotransduction mechanisms and promote the deposition of the anisotropically organized ECM that resembles that of native tendons.

These constructs can be used for mechanical augmentation or as complete replacement of injured tendon tissues and there are commercially available magnetotherapy devices that could be explored to implement this stimulatory approach in clinical scenarios. However, tendons midsubstance anchor to the adjacent bone or muscle through interface regions known as the enthesis and myotendinous junction, respectively.⁹³ Given the heterogeneity and biomechanical gradients present in these interfaces, the design of our scaffold might need further development to increase their potential for an effective insertion into bone or muscle, if it is to be used as a complete replacement. In either situation, *in vivo* studies using clinically relevant models of tendon injury will need to be conducted to quantitatively evaluate their regenerative performance. Moreover, DT-NP will likely be released from the scaffolds as they degrade over time. Despite their low content in the scaffolds (5 wt%) and although both main components of our hybrid magnetic nanoparticles (iron oxide MNP and CNC) have been showing a profile of biological safety,^{94,95} their actual *in vivo* fate after construct implantation should also be considered in future studies.

4. Conclusions

Scaffolds that replicate the architecture and biomechanical behavior of native tissue and are capable of being remotely actuated to mechanically stimulate cells toward regenerative profiles are of great interest in tendon TE strategies. To address this challenge, we have developed hybrid rod-shaped magnetic nanoparticles that simultaneously provide mechanical reinforcement and magnetic responsiveness to tendon biomimetic fibrous scaffolds fabricated by electrospinning and textile technologies. Importantly, it was demonstrated that the intrinsic physical cues of the tendon mimetic scaffolds combined with remote magneto-mechanical stimulation can steer hASC mechanotransduction mechanisms that boost their tenogenic differentiation and have a positive impact on the expression trends of anti-inflammatory/pro-healing and matrix remodeling gene markers. The potential application of the proposed system in *in vivo* settings for contactless cell mechanomodulatory stimulation can therefore contribute to direct the fate of seeded or recruited stem cells toward the tenogenic phenotype (or its maintenance in resident tenocytes), promote the deposition of the tendon-like ECM and control the host response after construct transplantation. Collectively, all these effects are expected to reduce tissue scarring at the injury site

during healing and ultimately improve the potential of TE strategies in the regeneration of functional tendon tissue.

Conflicts of interest

There are no conflicts to declare.

Acknowledgements

The authors would like to thank Hospital da Prelada (Porto, Portugal) for providing lipoaspirate surplus samples. The authors acknowledge the financial support from Fundação para a Ciência e Tecnologia for the SFRH/BPD/112459/2015 grant, the project SmarTendon-PTDC/NAN-MAT/30595/2017, the project MagTT PTDC/CTM-CTM/29930/2017, and the BPD_RL2_DECEMBER_2017 fellowship from NORTE-01-0145-FEDER-000021 supported by Norte Portugal Regional Operational Programme (NORTE 2020). The authors also acknowledge the financial support from the European Union Framework Programme for Research and Innovation HORIZON 2020, under the TEAMING Grant agreement No. 739572 – The Discoveries CTR, and the European Research Council 2017-CoG MagTendon (No. 772817).

References

- M. Schneider, P. Angele, T. A. H. Järvinen and D. Docheva, *Adv. Drug Delivery Rev.*, 2018, **129**, 352–375.
- A. J. Lomas, C. N. M. Ryan, A. Sorushanova, N. Shologu, A. I. Sideri, V. Tsioli, G. C. Fthenakis, A. Tzora, I. Skoufos, L. R. Quinlan, G. O’Laighin, A. M. Mullen, J. L. Kelly, S. Kearns, M. Biggs, A. Pandit and D. I. Zeugolis, *Adv. Drug Delivery Rev.*, 2015, **84**, 257–277.
- R. Costa-Almeida, A. I. Gonçalves, P. Gershovich, M. T. Rodrigues, R. L. Reis and M. E. Gomes, in *Tissue-Specific Stem Cell Niche*, ed. K. Turksen, Springer International Publishing, 2015, pp. 221–244.
- P. Kannus and P. Kannus, *Scand. J. Med. Sci. Sports*, 2000, **10**, 312–320.
- R. M. A. Domingues, A. I. Gonçalves, R. Costa-Almeida, M. T. Rodrigues, R. L. Reis and M. E. Gomes, in *Tendon Regeneration Understanding tissue physiology and development to engineer functional substitutes*, ed. M. E. Gomes, R. L. Reis and M. T. Rodrigues, Academic Press, 2015, pp. 259–280.
- J. H. C. Wang, *J. Biomech.*, 2006, **39**, 1563–1582.
- J. G. Snedeker and J. Foolen, *Acta Biomater.*, 2017, **63**, 18–36.
- D. L. Butler, N. Juncosa and M. R. Dressler, *Annu. Rev. Biomed. Eng.*, 2004, **6**, 303–329.
- G. Walden, X. Liao, S. Donell, M. J. Raxworthy, G. P. Riley and A. Saeed, *Tissue Eng., Part B*, 2017, **23**, 44–58.
- P. W. Ackermann, in *Tendon Regeneration Understanding tissue physiology and development to engineer functional substitutes*, ed. M. E. Gomes, R. L. Reis and M. T. Rodrigues, Academic Press, 2015, pp. 113–147.
- M. L. Santos, M. T. Rodrigues and R. M. A. Domingues, in *Regenerative Strategies for the Treatment of Knee Joint Disabilities*, ed. M. Oliveira and R. L. Reis, Springer International Publishing, 2017, vol. 21, pp. 349–371.
- N. Bölgen, in *Electrospun Materials for Tissue Engineering and Biomedical Applications: Research, Design and Commercialization*, ed. T. Uyar and E. Kny, Woodhead Publishing, 2017, pp. 233–260.
- M. Laranjeira, R. M. A. Domingues, R. Costa-Almeida, R. L. Reis and M. E. Gomes, *Small*, 2017, **13**, 1700689.
- M. T. Galloway, A. L. Lalley and J. T. Shearn, *J. Bone Jt. Surg., Am. Vol.*, 2013, **95**, 1620–1628.
- C. K. Kuo and R. S. Tuan, *Tissue Eng., Part A*, 2008, **14**, 1615–1627.
- N. Juncosa-Melvin, K. S. Matlin, R. W. Holdcraft, V. S. Nirmalanandhan and D. L. Butler, *Tissue Eng.*, 2007, **13**, 1219–1226.
- G. Yang, H.-J. Im and J. H.-C. Wang, *Gene*, 2005, **363**, 166–172.
- S. Dupont, *Exp. Cell Res.*, 2016, **343**, 42–53.
- M. T. Rodrigues, R. L. Reis and M. E. Gomes, *J. Tissue Eng. Regener. Med.*, 2012, **7**, 673–686.
- B. D. Riehl, J.-H. Park, I. K. Kwon and J. Y. Lim, *Tissue Eng., Part B*, 2012, **18**, 288–300.
- W. Liu, J. Lipner, C. H. Moran, L. Feng, X. Li, S. Thomopoulos and Y. Xia, *Adv. Mater.*, 2015, **27**, 2583–2588.
- L. J. Santos, R. L. Reis and M. E. Gomes, *Trends Biotechnol.*, 2015, **33**, 471–479.
- P. Cai, B. Hu, W. R. Leow, X. Wang, X. J. Loh, Y. L. Wu and X. Chen, *Adv. Mater.*, 2018, **30**, 1800572.
- Y. Sapir-Lekhovitser, M. Y. Rotenberg, J. Jopp, G. Friedman, B. Polyak and S. Cohen, *Nanoscale*, 2016, **8**, 3386–3399.
- A. I. Gonçalves, M. S. Miranda, M. T. Rodrigues, R. L. Reis and M. E. Gomes, *Biomed. Mater.*, 2018, **13**, 054001.
- Y. Sapir, S. Cohen, G. Friedman and B. Polyak, *Biomaterials*, 2012, **33**, 4100–4109.
- Y. Sapir, B. Polyak and S. Cohen, *Nanotechnology*, 2014, **25**, 014009.
- A. Tay, A. Sohrabi, K. Poole, S. Seidlits and D. Di Carlo, *Adv. Mater.*, 2018, **30**, 1800927.
- C. A. Cezar, E. T. Roche, H. H. Vandenburgh, G. N. Duda, C. J. Walsh and D. J. Mooney, *Proc. Natl. Acad. Sci. U. S. A.*, 2016, **113**, 1534–1539.
- U. D’Amora, T. Russo, A. Gloria, V. Riviaccio, V. D’Anto, G. Negri, L. Ambrosio and R. De Santis, *Bioact. Mater.*, 2017, **2**, 138–145.
- S. Hao, J. Meng, Y. Zhang, J. Liu, X. Nie, F. Wu, Y. Yang, C. Wang, N. Gu and H. Xu, *Biomaterials*, 2017, **140**, 16–25.
- J. Meng, B. Xiao, Y. Zhang, J. Liu, H. Xue, J. Lei, H. Kong, Y. Huang, Z. Jin, N. Gu and H. Xu, *Sci. Rep.*, 2013, **3**, 2655.
- R. K. Singh, K. D. Patel, J. H. Lee, E. J. Lee, J. H. Kim, T. H. Kim and H. W. Kim, *PLoS One*, 2014, **9**, e91584.

- 34 A. I. Gonçalves, M. T. Rodrigues, P. P. Carvalho, M. Bañobre-López, E. Paz, P. Freitas and M. E. Gomes, *Adv. Healthcare Mater.*, 2016, **5**, 213–222.
- 35 L. Santos, M. Silva, A. I. Gonçalves, T. Pesqueira, M. T. Rodrigues and M. E. Gomes, *Nanomedicine*, 2016, **11**, 1107–1122.
- 36 J. D. Rees, M. Stride and A. Scott, *Br. J. Sports Med.*, 2014, **48**, 1553–1557.
- 37 S. Araújo-Custódio, M. Gomez-Florit, A. R. Tomás, B. B. Mendes, P. S. Babo, S. M. Mithieux, A. S. Weiss, R. Domingues, R. L. Reis and M. E. Gomes, *ACS Biomater. Sci. Eng.*, 2019, **5**, 1392–1404.
- 38 T. Rada, R. L. Reis and M. E. Gomes, *J. Tissue Eng. Regener. Med.*, 2009, **3**, 158–159.
- 39 P. P. Carvalho, X. Wu, G. Yu, I. R. Dias, M. E. Gomes, R. L. Reis and J. M. Gimble, *Cells Tissues Organs*, 2011, **194**, 494–500.
- 40 P. P. Carvalho, X. Wu, G. Yu, M. Dietrich, I. R. Dias, M. E. Gomes, R. L. Reis and J. M. Gimble, *Cytotherapy*, 2011, **13**, 594–597.
- 41 K. J. Livak and T. D. Schmittgen, *Methods*, 2001, **25**, 402–408.
- 42 R. M. A. Domingues, S. Chiera, P. Gershovich, A. Motta, R. L. Reis and M. E. Gomes, *Adv. Healthcare Mater.*, 2016, **5**, 1364–1375.
- 43 P. Dhar, A. Kumar and V. Katiyar, *ACS Appl. Mater. Interfaces*, 2016, **8**, 18393–18409.
- 44 T. G. Barclay, H. M. Hegab, S. R. Clarke and M. Ginic-Markovic, *Adv. Mater. Interfaces*, 2017, **4**, 1601192.
- 45 Q. Zhu and Q. Pan, *ACS Nano*, 2014, **8**, 1402–1409.
- 46 J. Yang, C.-R. Han, J.-F. Duan, M.-G. Ma, X.-M. Zhang, F. Xu, R.-C. Sun and X.-M. Xie, *J. Mater. Chem.*, 2012, **22**, 22467–22480.
- 47 A. Cipitria, A. Skelton, T. R. Dargaville, P. D. Dalton and D. W. Huttmacher, *J. Mater. Chem.*, 2011, **21**, 9419–9453.
- 48 R. M. A. Domingues, M. E. Gomes and R. L. Reis, *Biomacromolecules*, 2014, **15**, 2327–2346.
- 49 N. Wei, Y. Jiang, Y. Ying, X. Guo, Y. Wu, Y. Wen and H. Yang, *RSC Adv.*, 2017, **7**, 11528–11536.
- 50 X. Zhang, M. Liu, Y. Zhang, B. Yang, Y. Ji, L. Feng, L. Tao, S. Li and Y. Wei, *RSC Adv.*, 2012, **2**, 12153.
- 51 N. Bhardwaj and S. C. Kundu, *Biotechnol. Adv.*, 2010, **28**, 325–347.
- 52 S. B. Orr, A. Chainani, K. J. Hippensteel, A. Kishan, C. Gilchrist, N. W. Garrigues, D. S. Ruch, F. Guilak and D. Little, *Acta Biomater.*, 2015, **24**, 117–126.
- 53 B. B. Rothrauff, B. B. Lauro, G. Yang, R. E. Debski, V. Musahl and R. S. Tuan, *Tissue Eng., Part A*, 2017, **23**, 378–389.
- 54 S. K. Czaplewski, T. Tsai, S. E. Duenwald-kuehl, R. Vanderby and W. Li, *Biomaterials*, 2014, **35**, 6907–6917.
- 55 L. A. Bosworth, N. Alam, J. K. Wong and S. Downes, *J. Mater. Sci. Mater. Med.*, 2013, **24**, 1605–1614.
- 56 S. Wu, Y. Wang, P. N. Streubel and B. Duan, *Acta Biomater.*, 2017, **62**, 102–115.
- 57 C. Erisken, X. Zhang, K. L. Moffat, W. N. Levine and H. H. Lu, *Tissue Eng., Part A*, 2013, **19**, 519–528.
- 58 N. M. Lee, C. Erisken, T. Iskratsch, M. Sheetz, W. N. Levine and H. H. Lu, *Biomaterials*, 2017, **112**, 303–312.
- 59 A. S. LaCroix, S. E. Duenwald-Kuehl, R. S. Lakes and R. Vanderby, *J. Appl. Physiol.*, 2013, **115**, 43–51.
- 60 Z. Yin, X. Chen, J. L. Chen, W. L. Shen, T. M. Hieu Nguyen, L. Gao and H. W. Ouyang, *Biomaterials*, 2010, **31**, 2163–2175.
- 61 C. Zhang, H. Yuan, H. Liu, X. Chen, P. Lu, T. Zhu, L. Yang, Z. Yin, B. C. Heng, Y. Zhang and H. Ouyang, *Biomaterials*, 2015, **53**, 716–730.
- 62 K. Spanoudes, D. Gaspar, A. Pandit and D. I. Zeugolis, *Trends Biotechnol.*, 2014, **32**, 474–482.
- 63 A. Totaro, T. Panciera and S. Piccolo, *Nat. Cell Biol.*, 2018, **20**, 888–899.
- 64 G. Halder, S. Dupont and S. Piccolo, *Nat. Rev. Mol. Cell Biol.*, 2012, **13**, 591–600.
- 65 T. P. Driscoll, B. D. Cosgrove, S. J. Heo, Z. E. Shurden and R. L. Mauck, *Biophys. J.*, 2015, **108**, 2783–2793.
- 66 S. Wan, X. Fu, Y. Ji, M. Li, X. Shi and Y. Wang, *Biomaterials*, 2018, **171**, 107–117.
- 67 M. Aragona, T. Panciera, A. Manfrin, S. Giullitti, F. Michielin, N. Elvassore, S. Dupont and S. Piccolo, *Cell*, 2013, **154**, 1047–1059.
- 68 M. Lavagnino, M. E. Wall, D. Little, A. J. Banes, F. Guilak and S. P. Arnoczky, *J. Orthop. Res.*, 2015, **33**, 813–822.
- 69 V. A. Codelia, G. Sun and K. D. Irvine, *Curr. Biol.*, 2014, **24**, 2012–2017.
- 70 S. Dupont, L. Morsut, M. Aragona, E. Enzo, S. Giullitti, M. Cordenonsi, F. Zanconato, J. Le Digabel, M. Forcato, S. Bicciato, N. Elvassore and S. Piccolo, *Nature*, 2011, **474**, 179–184.
- 71 S. Hughes, S. McBain, J. Dobson and A. J. El Haj, *J. R. Soc., Interface*, 2008, **5**, 855–863.
- 72 T. Pesqueira, R. Costa-Almeida and M. E. Gomes, *Sci. Rep.*, 2017, **7**, 10948.
- 73 Y. Liu, C. W. Suen, J. F. Zhang and G. Li, *J. Orthop. Transl.*, 2017, **9**, 28–42.
- 74 A. I. Gonçalves, M. T. Rodrigues, R. L. Reis and M. E. Gomes, in *In Situ Tissue Regeneration: Host Cell Recruitment and Biomaterial Design*, ed. S. J. Lee, J. J. Yoo and A. Atala, Elsevier Inc., 2016, pp. 275–293.
- 75 C. Shukunami, A. Takimoto, Y. Nishizaki, Y. Yoshimoto, S. Tanaka, S. Miura, H. Watanabe, T. Sakuma, T. Yamamoto, G. Kondoh and Y. Hiraki, *Sci. Rep.*, 2018, **8**, 3155.
- 76 X. Chen, Z. Yin, J. Chen, W. Shen, H. Liu, Q. Tang, Z. Fang, L. Lu, J. Ji and H. Ouyang, *Sci. Rep.*, 2012, **2**, 977.
- 77 D. Docheva, E. B. Hunziker, R. Fassler and O. Brandau, *Mol. Cell Biol.*, 2005, **25**, 699–705.
- 78 T. Komori, *Cell Tissue Res.*, 2010, **339**, 189–195.
- 79 A. Subramanian and T. F. Schilling, *Development*, 2015, **142**, 4191–4204.
- 80 M. E. Davis, J. P. Gumucio, K. B. Sugg, A. Bedi and C. L. Mendias, *J. Appl. Physiol.*, 2013, **115**, 884–891.

- 81 J. Foolen, S. L. Wunderli, S. Loerakker and J. G. Snedeker, *Matrix Biol.*, 2018, **65**, 14–29.
- 82 J. Lin, W. Zhou, S. Han, V. Bunpetch, K. Zhao, C. Liu, Z. Yin and H. Ouyang, *Acta Biomater.*, 2018, **70**, 1–11.
- 83 M. E. Ogle, C. E. Segar, S. Sridhar and E. A. Botchwey, *Exp. Biol. Med.*, 2016, **241**, 1084–1097.
- 84 T. U. Luu, S. C. Gott, B. W. K. Woo, M. P. Rao and W. F. Liu, *ACS Appl. Mater. Interfaces*, 2016, **7**, 28665–28672.
- 85 F. Y. McWhorter, T. Wang, P. Nguyen, T. Chung and W. F. Liu, *Proc. Natl. Acad. Sci. U. S. A.*, 2013, **110**, 17253–17258.
- 86 M. Tsuzaki, G. Guyton, W. Garrett, J. M. Archambault, W. Herzog, L. Almekinders, D. Bynum, X. Yang and A. J. Banes, *J. Orthop. Res.*, 2003, **21**, 256–264.
- 87 M. Stein, *J. Exp. Med.*, 1992, **176**, 287–292.
- 88 D. F. Fiorentino, A. Zlotnik, T. R. Mosmann, M. Howard and A. O'Garra, *J. Immunol.*, 1991, **147**, 3815–3822.
- 89 Y. Li, M. Ramcharan, Z. Zhou, D. J. Leong, T. Akinbiyi, R. J. Majeska and H. B. Sun, *Sci. Rep.*, 2015, **5**, 1–12.
- 90 A. E. C. Nichols, R. E. Settlage, S. R. Werre and L. A. Dahlgren, *BMC Cell Biol.*, 2018, **19**, 14.
- 91 H.-M. Yun, S.-J. Ahn, K.-R. Park, M.-J. Kim, J.-J. Kim, G.-Z. Jin, H.-W. Kim and E.-C. Kim, *Biomaterials*, 2016, **85**, 88–98.
- 92 A. Nakamura, Y. Dohi, M. Akahane, H. Ohgushi, H. Nakajima, H. Funaoka and Y. Takakura, *Tissue Eng., Part C*, 2009, **15**, 169–180.
- 93 S. F. Tellado, E. R. Balmayor and M. Van Griensven, *Adv. Drug Delivery Rev.*, 2015, **94**, 126–140.
- 94 N. Feliu, D. Docter, M. Heine, P. del Pino, S. Ashraf, J. Kolosnjaj-Tabi, P. Macchiarini, P. Nielsen, D. Alloyeau, F. Gazeau, R. H. Stauber and W. J. Parak, *Chem. Soc. Rev.*, 2016, **45**, 2440–2457.
- 95 A. B. Seabra, J. S. Bernardes, W. J. Fávaro, A. J. Paula and N. Durán, *Carbohydr. Polym.*, 2018, **181**, 514–527.